Modeling the transverse connection of fully precast steel-UHPC lightweight composite bridge

Shuwen Deng [1,2a], Zhiming Huang [2b], Guangqing Xiao [3c] and Lian Shen[*4]

[1] *College of Civil Engineering, Hunan University, Changsha 410082, China*
[2] *College of Water Resource & Civil Engineering, Hunan Agriculture University, Changsha 410025, China*
[3] *Guangdong Shengxiang Traffic Engineering Testing Co., Ltd., Guangzhou 510000, China*
[4] *Department of Civil Engineering, Changsha University, Changsha 410022, China*

Abstract. In this study, the modeling of the transverse connection of fully precast steel-UHPC (Ultra-High-Performance Concrete) lightweight composite bridges were conducted. The transverse connection between precast components plays a critical role in the overall performance and safety of the bridge. To achieve an accurate and reliable simulation of the interface behavior, the cohesive model in ABAQUS was employed, considering both bending-tension and compression-shear behaviors. The parameters of the cohesive model are obtained through interface bending and oblique shear tests on UHPC samples with different surface roughness. By validating the numerical simulation against actual joint tests, the effectiveness and accuracy of the proposed model in capturing the interface behavior of the fully precast steel-UHPC lightweight composite bridge were demonstrated.

Keywords: bridge connections; cohesive model; interfacial properties; numerical simulation method; ultra-high-performance concrete (UHPC)

1. Introduction

Prefabricated modular bridge serve as a significant avenue for achieving the industrialization of bridge construction (Larsson *et al.* 2014). However, these bridges have long been plagued by two formidable challenges: (1) Traditional concrete-based bridge structures are highly susceptible to cracking during usage, thereby causing water infiltration and giving rise to durability issues (Hájek *et al.* 2020, Katman *et al.* 2022), (2) Despite the ability to prefabricate the beam elements within a factory setting, on-site processes such as welding assembly, prestressing installation, and wet joint pouring remain indispensable, leading to protracted construction timelines and imposing substantial disruptions to the surrounding traffic environment. The aforementioned issues significantly hamper bridge operational efficiency, which is of particular urgency in the face of mounting heavy traffic volumes.

To address the aforementioned challenges, the incorporation of ultra-high-performance concrete (UHPC), characterized by exceptional strength, resilience, and durability (Ganesh and Murthy 2019, Dadmand *et al.* 2020, Pham *et al.* 2020, Mosaberpanah and Eren 2017), has been introduced into the construction of prefabricated modular bridges of medium and small spans, giving rise to a novel fully prefabricated steel-UHPC lightweight composite bridge (hereafter referred to as "LWCB"), as depicted in

Fig. 1. The LWCB consists of multiple preassembled steel-UHPC lightweight composite beams, which are connected by longitudinally and transversely joints. The construction process primarily encompasses the following stages: i) fabrication of lightweight composite beam units within a controlled factory environment, ii) transportation to the construction site for precise lifting and positioning, iii) installation of joint connecting rebars without the need for welding or tying, and iv) pouring of UHPC at the joints; and ultimately, completion of the construction process.

Compared to traditional prefabricated modular bridges with equivalent spans and technical standards, the LWCB offers significant advantages while maintaining a comparable initial cost (approximately 3900 *yuan*/m^2) (Zhao *et al.* 2019b, Deng *et al.* 2021). It achieves a substantial reduction in self-weight (reduced by 45%~65%) and beam height (reduced by 19%~26%). The lighter weight enables easy transportation and lifting using existing equipment and techniques, while the lower beam height allows for shorter approach spans and reduced pier heights, resulting in significant economic benefits in bridge selection for applications such as highway crossovers and multi-level urban viaducts. Furthermore, the exceptional durability of the LWCB leads to significantly lower maintenance costs compared to traditional solutions. Considering long-term performance, the LWCB demonstrates evident advantages in terms of economy, constructability, and durability.

In the case of prefabricated continuous bridges, the joint in the negative moment region represents a critical weak point in the structure. Numerous studies have explored the

---

*Corresponding author, Ph.D., Professor,
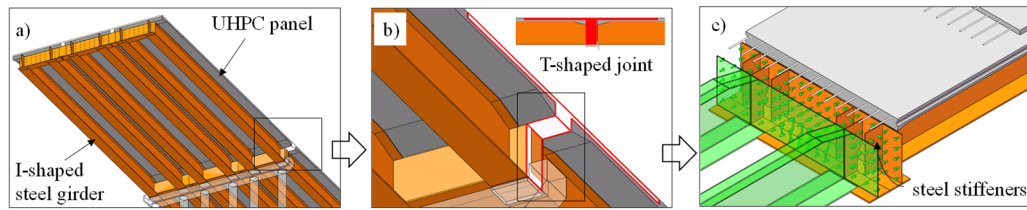E-mail: shenlian.lcz@163.com

Fig. 1 Schematic diagram of LWCB: (a) LWCB; (b) transverse joint; and (c) internal view of transverse joint

feasibility of using UHPC as a joint material, with a focus on its application in longitudinal and transverse joints for large-span steel bridge decks and longitudinal joints between panels in medium and small-span bridges. Studies related to joints suitable for large-span steel bridge decks typically investigate different joint forms, the reinforcement of bottom-profiled steel plates, and welded steel mesh to evaluate their impact on joint load transfer performance and efficiency (Qi *et al*. 2020, Lu *et al*. 2021, Pan *et al*. 2016, Shao *et al*. 2017, He *et al*. 2019, Jia *et al*. 2023, Xiao *et al*. 2022, Qi *et al*. 2019, Du *et al*. 2022, Zhao *et al*. 2019a). Research on longitudinal joints between panels in medium and small-span bridges generally examines different joint forms, interface treatment methods, and internal reinforcement configurations to assess their influence on joint crack resistance and failure modes (Chitty *et al*. 2020, Abokifa and Moustafa 2021, Deng *et al*. 2023, Graybeal 2014, He *et al*. 2013, Jiang *et al*. 2022, Qiu *et al*. 2022, Shah *et al*. 2021, Zhu *et al*. 2020a, Tan *et al*. 2022, Shao *et al*. 2021).

In previous work, the authors conducted experimental and theoretical analyses on negative moment joints in LWCB (Deng *et al*. 2020, 2021). In order to obtain more extensive research results (including improved strength and optimized structural design), it is necessary to establish an accurate finite element model. Therefore, this study focuses on numerical simulations of T-shaped beam joints located on top of bridge piers applied in the Mapu Bridge. An interface cohesive model is employed to simulate the behavior of UHPC joint interfaces, which is specifically tailored for prefabricated structures. The model utilizes conventional contact setting methods and specifies different parameters based on the interface roughness. To obtain simulation parameters between successively cast UHPCs, bending and oblique shear tests were carried out on successively cast UHPC samples. Subsequently, the numerical model of Mapu Bridge T-shaped beam joint was established, providing a valuable methodological reference for further research.

2. Literature review

The finite element simulation of NC-NC or UHPC-NC interfaces has been extensively investigated in previous studies (Bayat *et al*. 2020, Hussein *et al*. 2022, Zhu *et al*. 2020b, c, d). Various approaches have been employed to model the interface behavior. Some researchers simplified the interface by assuming complete bonding (tie) (Júlio *et al*. 2006, Wall and Shrive 1988, Ulku *et al*. 2010). Others

introduced a bonding material between the interfaces and obtained interface material parameters through experimental fitting (Farzad *et al*. 2019, Porter *et al*. 2011). Additionally, some studies utilized the friction coefficient between the interfaces (Grace *et al*. 2008, 2013) Dias da Costa (Dias-da-Costa *et al*. 2012) employed a zero-thickness linear contact element to simulate the joint surface.

In the context of finite element analysis of UHPC joints applicable to prefabricated structures, Chen (Chen and Graybeal 2012b) conducted a simulation of UHPC prestressed π-beams with joints. The joint interface was modeled as a hard contact in the normal direction and a friction coefficient in the tangential direction. Chen emphasized that complete bonding (tie) cannot accurately simulate the behavior between joints and beam bodies. Grace (Grace *et al*. 2013) simulated five T-beams using UHPC as shear connectors through the finite element method, assuming fully bonded joints. The simulation results were compared with experimental data. Steinberg (Steinberg *et al*. 2013) performed simulations on the shear key between adjacent box girders, considering a friction coefficient of 0.8 and a shear stress of 5.5 MPa between the shear key and the box girder. The contact stiffness between concrete was set to 2.7 MPa/mm, and between UHPC and ordinary concrete, it was 13.6 MPa/mm. However, some deviation was observed between the model and the experimental results. Harries (Harris *et al*. 2015) used complete bonding to simulate the interface behavior in UHPC-NC composite splitting, oblique shear, and pull-out tests. Hussein (Hussein *et al*. 2017b) employed the cohesive model to fit the UHPC-HPC interface behavior, obtaining parameters for different interface roughness conditions. Jang (Jang *et al*. 2018) conducted push-out tests on UHPC joints and used the cohesive model to obtain fitting parameters by comparing the test beams.

The method of complete bonding represents an upper limit state of interface connection. Test results from references (Carbonell *et al*. 2013, Liao 2018, Harris *et al*. 2015) indicate that when the interface is rough, failure occurs within the NC matrix, allowing for the assumption of complete bonding. However, for medium rough or smooth interfaces, adopting complete bonding can lead to an overestimation of specimen bearing capacity and yield incorrect conclusions. When considering only the friction coefficient, as described in the calculation formula (1) from Birkeland (Birkeland and Birkeland 1966), which includes shear strength (v_n), interface friction coefficient (μ), and shear reinforcement yield strength (f_y), the influence of cohesion between the interfaces is neglected. Nevertheless,

numerous tests have demonstrated the existence of adhesion forces, even for smooth interfaces, and thus, solely relying on the friction coefficient will underestimate the bearing capacity of the specimen. Chen (Chen and Graybeal 2011) attempted to combine a hard contact with a default coefficient and friction coefficient, but this approach does not take into account the specific characteristics of the interface. Based on the aforementioned test results, it becomes evident that cohesion and friction coefficients vary between smooth, medium rough, and particularly rough interfaces, rendering this method non-universal. Steinberg (Steinberg *et al*. 2013) employed a parameter setting method that involved multiple parameters, but the results were unsatisfactory.

$$v_n = \mu \rho f_y \qquad (1)$$

Setting the interface bonding material is considered a relatively ideal method. The parameters of the interface material can be determined through testing. Farzad (Farzad *et al*. 2019) obtained the elastic modulus, Poisson's ratio, and concrete damage plastic parameters of the UHPC-NC composite specimen's interface material by conducting bending tension, direct shear, and oblique shear tests. Although he set the interface thickness to 100 μm, no further explanation was provided for this value. Similar conclusions were reached by Han (Han 2002, Han *et al*. 2004) in their investigation of the failure mode of the bonding surface between pre-cast and post-cast concrete. They defined this interface layer as the fracture process area and derived the calculation formula (2) for the length of the fracture process area through a combination of experimental testing and theoretical analysis.

$$l = \frac{3}{2\pi}\left(\frac{K_{Ic}}{f_t{}'}\right)^2 \qquad (2)$$

In the formula, K_{Ic} is bond fracture toughness, $f_t{}'$ is the tensile strength of the interface layer. Both parameters are characteristics of the interface material and require determination through experimental testing. As reported by Han (Han 2002, Han *et al*. 2004), the length of the fracture process zone between pre-cast and post-cast concrete was found to be 26.4 mm, which significantly differs from the value obtained by Farzad (Farzad *et al*. 2019) as mentioned earlier. Furthermore, when dealing with joint interfaces of special shapes (e.g., sawtooth, dovetail, etc.), establishing a distinct interface layer alone can become challenging.

To simulate interface cracking in composite structures, dynamic crack propagation in brittle materials, and crack initiation between thin film coatings on a ductile matrix, the cohesive model has been widely utilized. Within ABAQUS (Systèmes 2010), there are two primary methods to define the cohesive model: one involves defining the cohesive element, which can be represented with zero thickness and is primarily used for damage simulation between multilayer composites, employing elements such as COH3D8 and COH3D6. The other approach is to set cohesive behavior based on the surface, which is a contact attribute. The theoretical foundation is akin to that of the cohesive
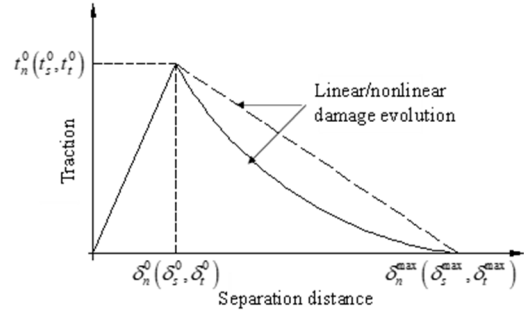

Fig. 2 Calculation diagram of cohesion model

element, but its definition is more straightforward compared to the cohesive element. A typical response of the cohesive model is illustrated in Fig. 2.

Where $t_n^0(t_s^0, t_t^0)$ is the maximum separation stress in three coordinate axis directions, $\delta_n^0(\delta_s^0, \delta_t^0)$ is the corresponding displacement, and $\delta_n^f(\delta_s^f, \delta_t^f)$ is the maximum separation distance. The elastic stage of the contact separation model can be expressed as formula (3).

$$t = \begin{Bmatrix} t_n \\ t_s \\ t_t \end{Bmatrix} = \begin{bmatrix} K_{nn} & K_{ns} & K_{nt} \\ K_{ns} & K_{ss} & K_{st} \\ K_{nt} & K_{st} & K_{tt} \end{bmatrix} \begin{Bmatrix} \delta_n \\ \delta_s \\ \delta_t \end{Bmatrix} = K\delta \qquad (3)$$

Where K is the contact stiffness matrix in the elastic stage, it includes three directions. Damage occurs when the cohesion reaches the peak point (i.e., t^0 in the above figure). The later stage of damage evolution can be expressed in linear or nonlinear form. It is worth noting that the damage here refers to the damage in contact properties rather than material property values. ABAQUS has four definitions of contact damage criteria: maximum stress criterion, maximum separation criterion, secondary stress criterion, and secondary separation criterion. The maximum stress criterion has a simple form and precise definition, and its expression is (4).

$$max\left\{\frac{\langle t_n \rangle}{t_n^0}, \frac{\langle t_s \rangle}{t_s^0}, \frac{\langle t_t \rangle}{t_t^0}\right\} = 1 \qquad (4)$$

In the above formula, damage occurs when the cohesion in any direction reaches the set maximum stress. The part of damage degradation in Fig. 2 can be expressed in linear or nonlinear form. In ABAQUS, D represents the damage at the contact point. This variable increases from 0 to 1, indicating that the damage begins to occur until it is completely damaged, as shown in formula (5).

$$\begin{cases} t_n = (1 - D_n)t_n^0 \\ t_s = (1 - D_s)t_s^0 \\ t_t = (1 - D_t)t_t^0 \end{cases} \qquad (5)$$

In order to represent the total separation value in three directions, we introduce δ_m. The calculation formula is (6)

$$\delta_m = \sqrt{\langle \delta_n \rangle^2 + \delta_s{}^2 + \delta_t{}^2} \qquad (6)$$

When the damage stage is set to linear, the damage D can be expressed as (7)

$$D = \frac{\delta_m^f \left(\delta_m^{max_0} () \right)}{\delta_m^{max} (\delta_m^f - \delta_m^0)} \quad (7)$$

When the damage is defined as nonlinear, the damage D can be expressed as (8)

$$D = 1 - \left\{ \frac{\delta_m^0}{\delta_m^{max}} \{\} \left\{ 1 - \frac{1 - exp\left(-\alpha \frac{\delta_m^{max_0}}{\delta_m^f - \delta_m^0} () \right)}{1 - exp(-\alpha)} \{\} \right\} \right\} \quad (8)$$

In the above calculation, δ_m^0 and δ_m^{max} represent the separation distance at the initial damage and the corresponding distance at the maximum damage, respectively. α is a dimensionless parameter representing the damage evolution rate, which can be adjusted according to the test results. It can be seen from the above expression that when defining the cohesive model, it is mainly necessary to determine the initial separation stress t_0 in three directions, the bonding stiffness K of the linear elastic section, the initial separation distance δ_0, and the maximum separation distance δ_{max}. If the nonlinear formula is used to calculate the damage D, the dimensionless parameter α needs to be determined.

Hussein (Hussein *et al.* 2017b) and Jang (Jang *et al.* 2018) utilized the cohesive model to simulate the interface contact behavior and proposed model parameters suitable for UHPC-HPC and UHPC-UHPC interfaces, respectively. These parameters include contact stiffness, initial separation strength, and plastic separation distance in three directions. The cohesive model allows for setting different parameters based on varying interface roughness, making it an ideal contact setting method. Thus, in this study, the cohesive model is employed to successfully fit the interface of poured UHPC joints. To achieve this, flexural and oblique shear tests were conducted on successively poured UHPC specimens to obtain simulation parameters required for different contact modes. Subsequently, numerical simulations of UHPC transverse joints, successively poured in an actual bridge section test, were carried out to verify the effectiveness of the obtained parameters.

3. Simulation of flexural-tensile behaviour of UHPC interface based on cohesive model

3.1 Numerical simulation procedure

The UHPC materials used in the test mainly consist of steel fiber, silica fume, and quartz sand. The pre-cast UHPC undergoes steam curing and contains 2.0% linear steel fiber, while the post-cast part of UHPC undergoes natural curing and includes 2.5% steel fiber (1% linear + 1.5% end hook). Flexural, compressive, and elastic modulus tests were

Table 1 Mechanical properties of UHPC materials

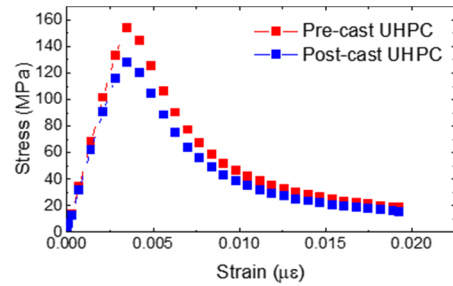| Material type	Curing method	Compressive strength (MPa)	Flexural strength (MPa)	Modulus of elasticity (GPa)
Pre-cast UHPC	Steam Curing	162.38	28.74	49.03
Post-cast UHPC	Natural curing	135.01	32.19	45.82

Fig. 3 UHPC Stress-strain diagram of UHPC material under pressure

conducted on both materials, and the test results are presented in Table 1.

For the finite element simulation, the CDP (Concrete Damaged Plasticity) model in ABAQUS is employed. The UHPC material constitutive model needs to be divided into two components: compression and tension. The constitutive compression model described in literature (Yang and Fang 2008) was adopted and can be expressed as follows (Eq. (9)).

$$\sigma_c = \begin{cases} f_c \dfrac{n\xi - \xi^2}{1 + (n-2)\xi} & \varepsilon \le \varepsilon_0 \\[2ex] f_c \dfrac{\xi}{2(\xi - 1)^2 + \xi} & \varepsilon > \varepsilon_0 \end{cases} \quad (9)$$

Where f_c is the compressive strength of UHPC, ξ is the strain ratio, $\xi = \frac{\varepsilon}{\varepsilon_0}$, $n = \frac{E_c}{E_{sec}}$, E_c is the initial elastic modulus, and E_{sec} is the secant modulus at the peak point. In this paper, the compressive strength was tested. For the prefabricated and post cast parts, it is $f_{c-pre} = 0.95 \times 162.38 = 154.26$ MPa and $f_{c-post} = 0.95 \times 135.01 = 128.26$ MPa, respectively. By reference (Yang and Fang 2008), the ε_0 is set to be 3500, and the initial elastic modulus is $E_{c-pre} = 49.03$ GPa and $E_{c-post} = 45.82$ GPa, respectively. According to the above formula, the compressive stress-strain curve of UHPC can be obtained, as shown in Fig. 3. For the tensile stress-strain relationship, the measured values of this test are used, and the tensile stress-strain curve is shown in Fig. 4.

To define the tensile and compressive stress-strain relationships of materials, the CDP model in ABAQUS requires the setting of parameters related to plasticity criterion, strengthening criterion, and flow rule. The values of these parameters can be found in reference (Cao 2016) and are summarized in Table 2.

Table 2 UHPC plastic damage model parameters

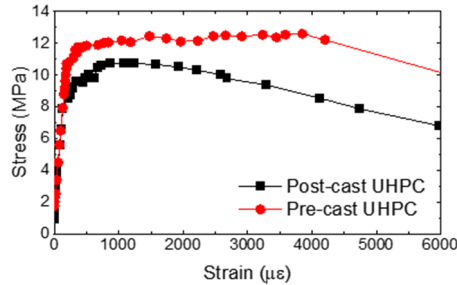| Dilation angle	Eccentricity coefficient	Biaxial compression / uniaxial compression	K	Viscosity coefficient
36	0.1	1.16	0.667	0

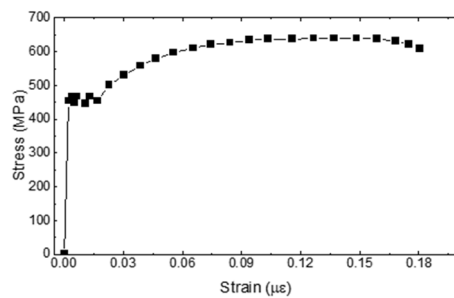Fig. 4 Tensile stress-strain diagram of UHPC material
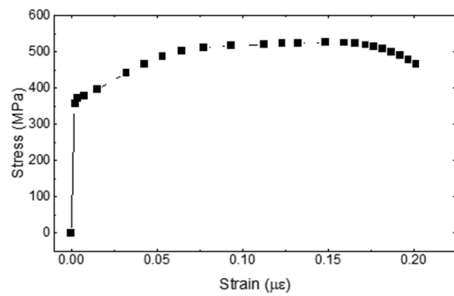

Fig. 5 Diagram of tensile stress-strain of reinforcement

Fig. 6 Q345 steel plate compression stress-strain diagram

Based on the test findings of successively poured UHPC joints by Deng *et al.* (2021), it was observed that the internal reinforcement of the test beam reached its yield strength during the later stages of loading. Therefore, for the finite element simulation, the test results of HRB400 reinforcement from (Zhao 2014) were utilized. The stress-strain constitutive relationship is depicted in Fig. 5. In (Zhao 2014), only the tensile strength of the reinforcement was tested. Considering the unique properties of reinforcement materials, it is assumed that the constitutive compression model is identical to the constitutive tension model.

Similarly, the stress-strain curve for Q345 steel was obtained from the tensile test conducted in (Chen and El-Hacha 2015). The study focused on investigating the properties of steel under different loading rates. For this paper, the quasi-static test was performed at a strain rate of 1.0×10^{-3} s^{-1}, as illustrated in Fig. 6. It is also assumed that
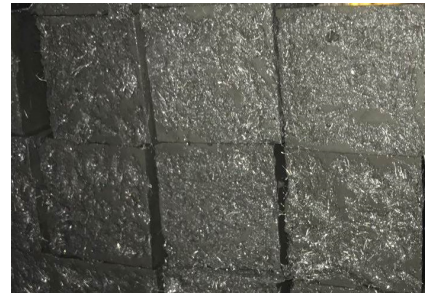

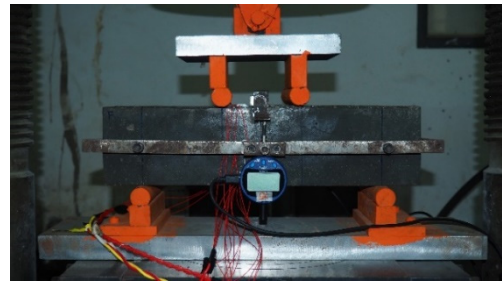Fig. 7 Roughened surface of UHPC interface in flexural test

Fig. 8 Loading and measurement scheme of flexural test

the compressive stress-strain relationship of the steel plate is equivalent to that observed in tension.

3.2 Bending test of successively poured UHPC

The prefabricated section of the test beam underwent steam curing, preceded by roughening the surface using a high-pressure water gun. The post-cast section was poured on the same day. Additionally, a batch of specimens with a smooth interface (without chiselling) was simultaneously poured to obtain fitting parameters for the finite element model for both rough and smooth interface conditions. The chiselled surface of the specimen is depicted in Fig. 7. The dimensions and mechanical properties of the specimens are identical to those used in the flexural tests. Each group consists of three specimens, with two groups having smooth and rough interfaces, respectively. During the tests, deflection of the test pieces and strain on all four surfaces were recorded. The loading and measurement scheme is illustrated in Fig. 8.

Throughout the tests, all specimens experienced failure at the interface. The failure modes of intact, smooth, and rough specimens are depicted in Fig. 9. In the smooth interface group, minimal evidence of bonding or exposed steel fibers is observed on the failure surface. In contrast, the rough interface group exhibits exposed steel fibers at the failure interface. However, it can be observed that some edges of the rough interface are not fully roughened, possibly causing the significant dispersion observed in the rough interface specimens as the edges are not as rough as the middle section. In the intact specimen group, numerous steel fibers are distributed on the failure surface. From a side view of the specimen, it can be seen that the failure surface of the fully bonded specimen features densely arranged longitudinal fibers, effectively bridging and impeding crack propagation. However, the crack surface of
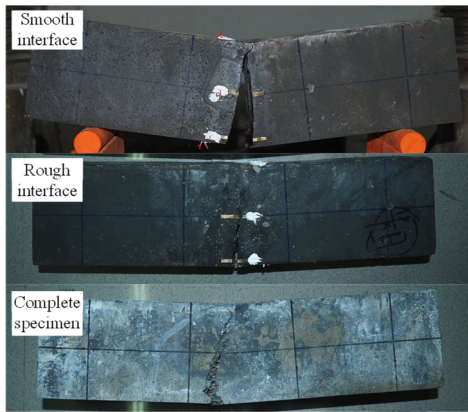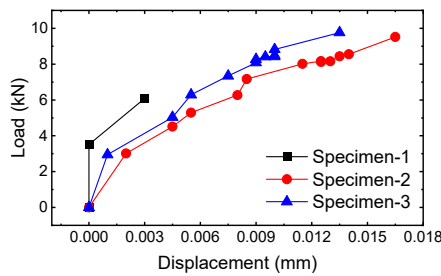
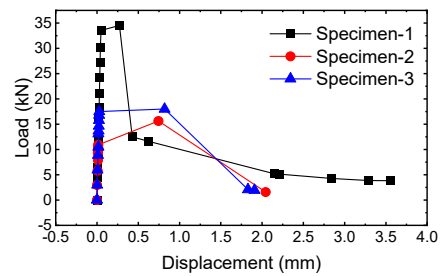(a) Side view of failure surface of flexural test
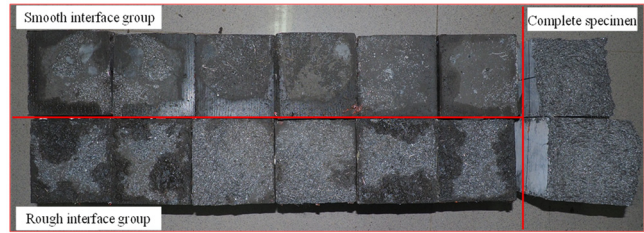
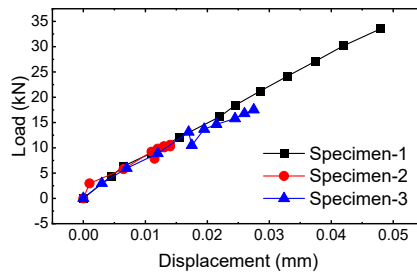(b) Front view of failure surface of flexural test

Fig. 9 Schematic diagram of failure surface of interface flexural test

(a) Smooth interface

(b) Rough interface

(c) Front section of rough interface

Fig. 10 Load-deflection curve of flexural test

the rough interface specimen shows almost no longitudinal fibers, with some matrix material being peeled off. In the case of the smooth interface specimen, failure occurs directly along the interface, with only partial peeling observed in the compression region.

Fig. 10 illustrates the load-displacement curves of specimens from the smooth and rough interface groups. To enhance clarity and focus on the deformation curve of the rough interface specimen, the linear section in the early stage of Fig. 10(b) is extracted and presented separately in Fig. 10(c).

From Fig. 10, it is evident that the ultimate bearing capacity of the smooth interface specimens is lower than that of the rough interface specimens. The failure loads of the three smooth specimens are 8.34 kN, 9.52 kN, and 9.78 kN, respectively. On the other hand, the failure load of the rough interface specimens exhibits some variation and demonstrates slight ductility, with ultimate loads of 34.52 kN, 15.62 kN, and 17.97 kN, respectively.

The strain behavior of the two specimen groups is presented in Fig. 11. As observed in the figure, the strain on the tension side exhibits more variation compared to the compression side, and the rough interface specimens display smoother and larger strain variations. This behavior is likely attributed to the uneven chiseling process. In the simulation of the joint specimens, considering the larger chiseling area and reinforcement, the test results of the rough surface group will be utilized.

3.3 UHPC Numerical simulation

The finite element model for the bending test is depicted in Fig. 12. The model utilizes C3D8R solid elements, which are eight-node hexahedral elements with three translational degrees of freedom. These elements are suitable for analyzing nonlinear phenomena such as large deformations, contact, and failure under complex stress conditions. To alleviate significant stress concentrations, steel plates were placed at the loading point. Translational degrees of freedom in the X, Y, and Z directions are constrained at the
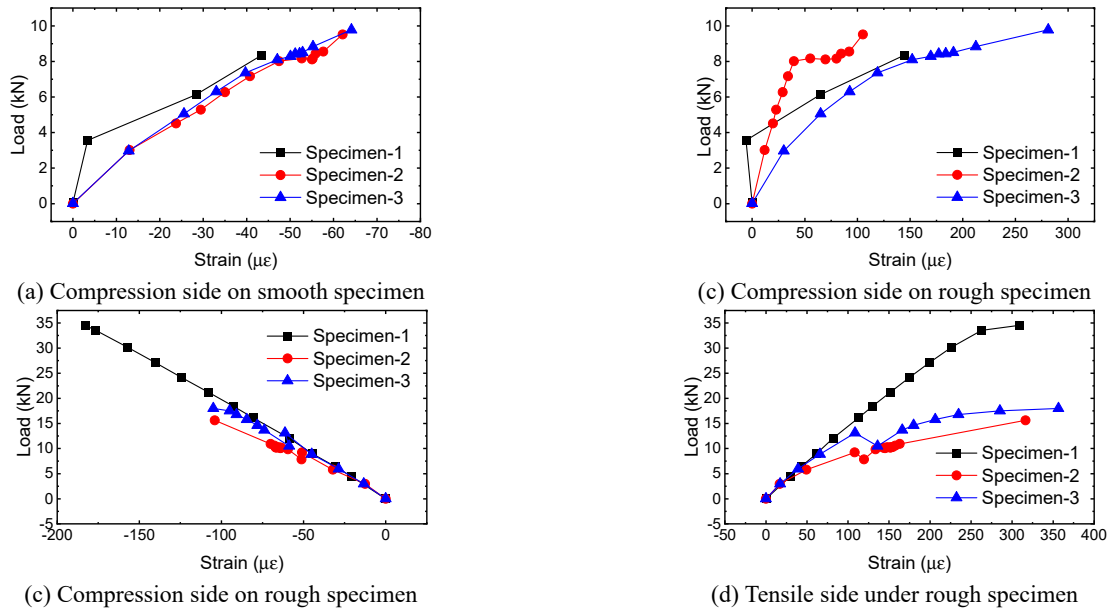
(a) Compression side on smooth specimen

(c) Compression side on rough specimen

(c) Compression side on rough specimen

(d) Tensile side under rough specimen

Fig. 11 Development curve of load-strain of flexural specimen

Table 3 Interface fitting parameters of flexural-tensile dominated components

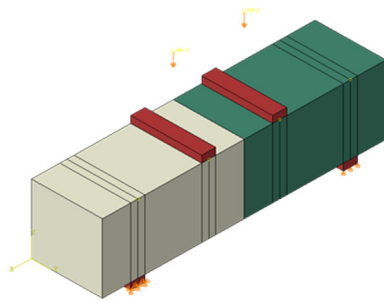| Interface form	$K_{nn}/K_{ss}/K_{tt}$	$t_n^0/t_s^0/t_t^0$ (MPa)	Δp (mm)	Viscosity coefficient	Calculation results (kN)	Test result (kN)
Smooth	45820/45820/45820	1.955/1.955/1.955	0.01667	1e-6	10.17	9.76
Rough	45820/45820/45820	6.716/6.716/6.716	0.0533	1e-6	34.47	34.52

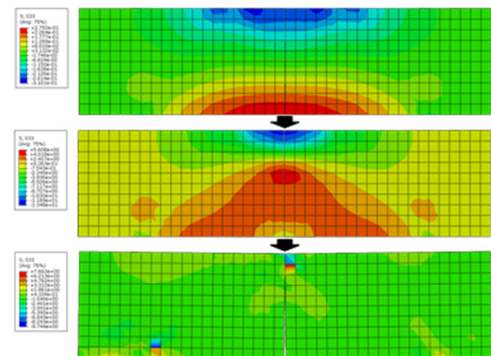Fig. 12 Finite element model of bending test

Fig. 13 Finite element fitting process of interface bending test

lower left of the specimen, while the right support only restricts degrees of freedom in the Y direction. An auxiliary loading point was established to apply the displacement load, and the element grid was set to 10 × 10 × 10 mm.

Consistent with the experimental setup, the mechanical properties of the specimens in the simulation are divided into smooth interface and rough interface groups. Since the test results of the two smooth interface specimens show minimal differences, specimen 2, which has a lower value, is selected to represent the smooth group in the simulation. Conversely, the rough interface group exhibits a significant dispersion in bearing capacity, likely due to uneven chiseling at the edges of the specimens. Thus, specimen 1, which has a higher bearing capacity, is chosen for the fitting process. Table 3 provides the cohesive parameters applicable to bending and tension for both the smooth and rough interface groups. The finite element calculation process is illustrated in Fig. 13.

In Fig. 14, the load-displacement curve and upper compression strain curve for both the smooth and rough interface groups are presented. These curves have been fitted, and the fitting results show excellent agreement with the experimental test data.

3.4 Discussion

In Table 3, the parameters are discussed as follows:

The contact stiffness values ($K_{nn}/K_{ss}/K_{tt}$) have a minor influence on the overall structural stiffness. Adjusting these values can slightly modify the slope of the load-displacement curve. Since the flexural specimen can only effectively determine the normal parameters, the two tangential stiffness values are set to be the same as the

(a) Load- displacement of specimens with smooth interface

(b) Compressive strain on the upper side of smooth interface specimens

(c) Load- displacement of specimen with rough interface

(d) Compressive strain on the upper side of rough interface specimens
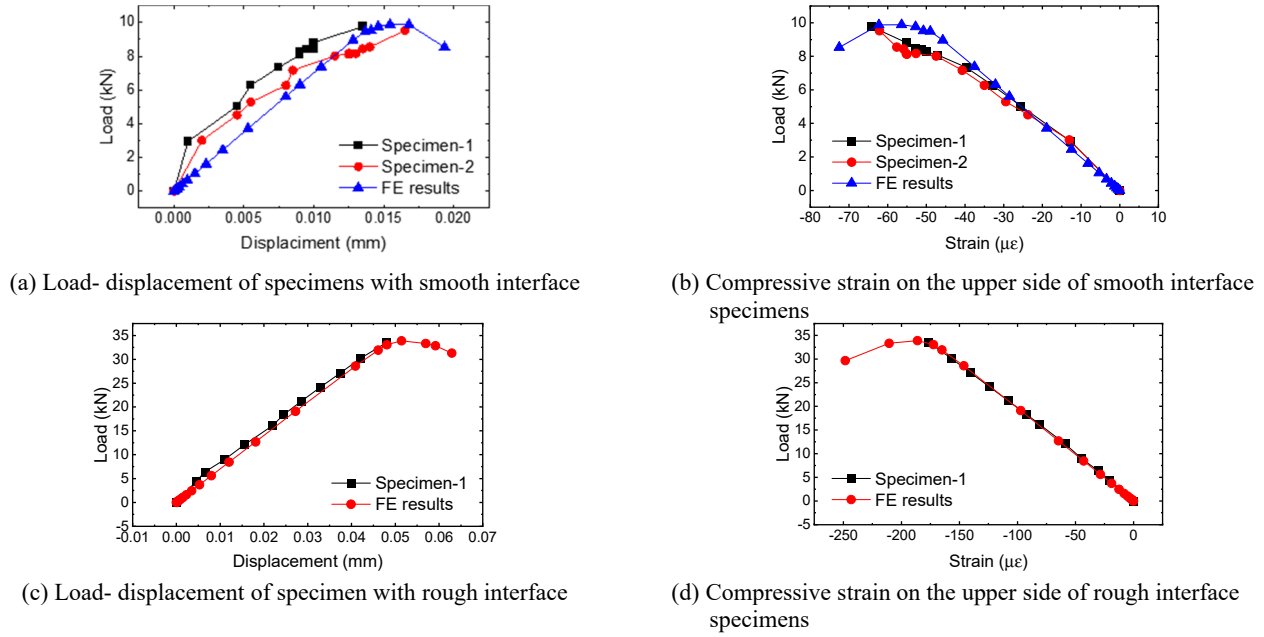
Fig. 14 Fitting results of finite element calculations and experimental results

normal stiffness, which aligns with the approach used in references (Jang *et al*. 2018, Hussein *et al*. 2017b).

The boundary conditions applied to the specimen have a significant impact on the simulation results. The level of restraint greatly affects the slope of the calculated load-displacement curve, thereby influencing the structural stiffness. It should be noted that when the specimen is fully restrained, the calculated bearing capacity in later stages may exceed the actual test results. The boundary condition setting method employed in this paper is considered to be one of the more reasonable approaches after thorough testing.

The selection of initial separation stress values ($t_n^0/t_s^0/t_t^0$) in Table 3 follows the method of back extrapolation of the load-displacement curve outlined in the French UHPC structure technical recommendation (AFGC-SETRA 2013). Taking the rough interface as an example, the elastic limit point F of the rough interface specimen is determined based on Fig. 9(b), and then the initial separation stress is calculated using the formula (10) as follows

$$f_{cr,dt} = f_{cr} \cdot \alpha \cdot a^{0.7}/(1 + \alpha \cdot a^{0.7}) \qquad (10)$$

Where $f_{cr,dt}$ is the flexural tensile initial crack strength. f_{cr} is flexural tensile initial crack strength. The value of α is 0.08, representing the reduction coefficient of the size effect. a is the height of the test piece. From this formula, it can be determined that the initial separation stress of the rough interface is 6.716 MPa. This value greatly influences the ultimate bearing capacity of the structure. The initial separation distance δ_0 is calculated references to Elices *et al*. (1992) as Fig. 15 and formula (11~15).

$$w = 2x \sin(\theta/2) \approx \theta x \qquad (11)$$
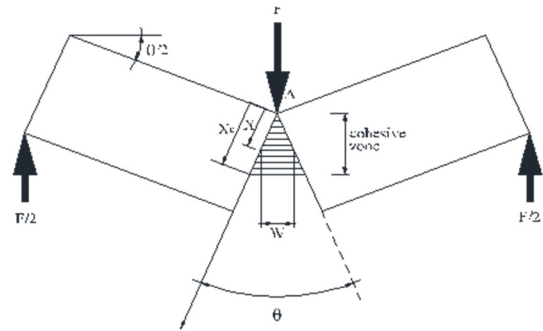
$$\theta = \frac{4\delta}{S} \qquad (12)$$

Fig. 15 Calculation diagram of initial separation distance

Here, takes the rough interface as an example. From the above two formulas, we can get

$$w_0 = 0.065 \times \frac{4}{300} \times 100 = 8.67 \times 10^{-3} \, mm \qquad (13)$$

$$w_{max} = 0.048 \times \frac{4}{300} \times 100 = 0.064 \, mm \qquad (14)$$

Thus, the total plastic separation distance is

$$\delta_p = \delta_{max}\delta_0 = 0.064 - 8.67 \times 10^{-3} = 0.05533 \, mm \ (15)$$

The selection of the initial separation distance (δ_0) can improve the calculated bearing capacity within a reasonable range. However, beyond this reasonable range, there is a significant increase in the falling section of the curve, which greatly enhances the bearing capacity during the stage of interfacial plastic failure. Conversely, choosing a value that is too small can lead to convergence difficulties in the calculation.

The viscosity coefficient also plays a crucial role in the calculation results and convergence. A larger coefficient in

Fig. 16 Surface roughening of oblique shear specimen in rough interface group

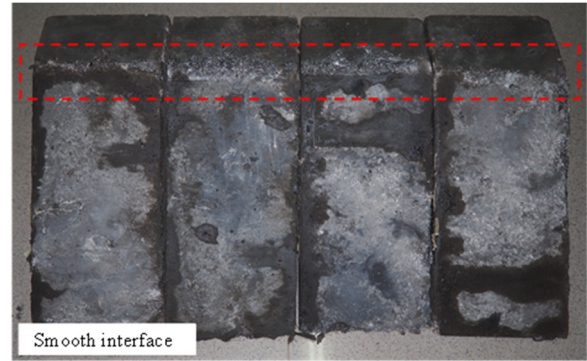Fig. 17 Schematic diagram of oblique shear specimen loading

(a) smooth interface

(b) rough interface

Fig. 18 Failure of oblique shear specimen

Table 4 Interface oblique shear test results (kN)

No.	1	2	3	Mean value
Smooth group	714.13	686.30	-	700.215
Rough group	1424.72	1110.33	1251.56	1262.203

the first half of the load-displacement curve can significantly increase the ultimate load and delay the onset of plastic deformation at the interface. In this paper, to minimize the influence of this coefficient, it is set to the minimum value of $1e^{-6}$.

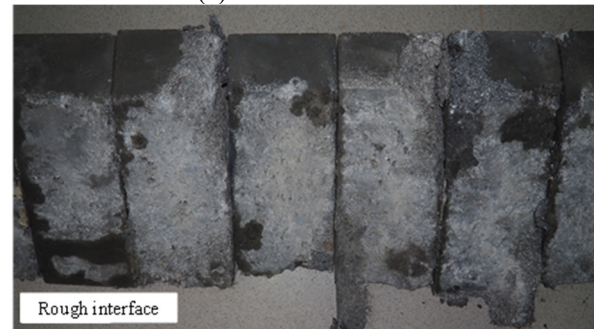## 4. Simulation of compression-shear behaviour of UHPC interface based on cohesive model

4.1 Test introduction

The materials used and the degree of surface roughening of the interface in the oblique shear test are the same as those in the flexural test. The specimen size is 300 × 100 × 100 mm, and the interface is poured successively at a skew angle of 30°. Each group consists of three specimens, with a total of six specimens for the smooth and rough interface groups. The chiselling process and the loading configuration of the specimen are illustrated in Fig. 16 and Fig. 17, respectively.

During the loading process, a 200 t press machine was utilized for the test. However, due to safety concerns, only five specimens (2 smooth interface and 3 rough interface) were tested. It is worth noting that during the test, the specimens produced a loud sound at the moment of failure, and a portion of the specimen even ejected from the setup, indicating a potentially hazardous situation. The failure surfaces of the specimens are depicted in Fig. 18. In the case of the smooth interface specimens (Fig. 18(a)), the failure occurred solely at the interface, with the damage limited to the specimen edges due to imprecise workmanship. No damage was observed in the central core region. Conversely, for the specimens with the rough interface (Fig. 18(b)), in addition to the evident shear failure at the interface, partial crushing of the matrix was also observed. Detailed test results can be found in Table 4.

4.2 Numerical simulation

The finite element fitting parameters for compression-shear members can be determined based on the test results of oblique shear specimens. These parameters align with the ones used in the previous bending-tensile tests. During the initial loading stage, the shear force is transmitted along the interface, and the cohesive model is activated to resist the increasing shear slip. As the load gradually increases, the cohesion reaches its peak value, and the contact damage is activated. Consequently, the contribution of the cohesion model to shear resistance diminishes. At this stage, the friction coefficient comes into play (Hussein *et al*. 2017a). Therefore, in addition to the parameters related to cohesion and damage, it is necessary to define the contact friction coefficient between interfaces. The normal and tangential stresses correspond to the maximum separation stresses in three directions. The values of normal stress, tangential stress, and friction coefficient can be determined using the
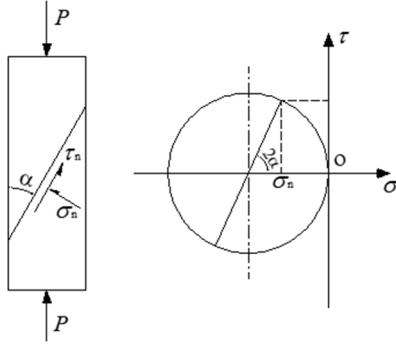
Fig. 19 Calculation of oblique shear specimen with Mohr-Coulomb circle

Table 5 Interface oblique shear test results (kN)

No.	σ_n (MPa)	τ_n (MPa)	c	μ
Smooth group	17.49	30.31	1.955	1.62
Rough group	31.53	54.64	6.716	1.52

Mohr-Coulomb theorem (Fig. 19) and formulas (16-18).

$$\sigma_n = \frac{P}{A} sin^2 \alpha \qquad (16)$$

$$\tau_n = 0.5 \frac{P}{A} sin(2\alpha) \qquad (17)$$

$$\tau_n = c + \mu\, \sigma_n \qquad (18)$$

In the above formula, σ_n is the normal stress at the interface. τ_n is the tangential stress at the interface. α is the interface skew angle. A is the cross-sectional area at the loading position. c is the bond strength. μ is the coefficient of friction. According to the above test, the average peak load corresponding to the two interfaces is 700.22 kN and 1262.20 kN. The normal stress, tangential stress and friction coefficient are shown in Table 5, calculated by the above formula.

The following is a concise description of the parameter fitting process, using the rough interface group as an example. Based on the previous description, t_{nn} = 31.53 MPa and $t_{ss} = t_{tt}$ = 54.64 MPa were obtained from Table 5. Referring to the results of the oblique shear test (Table 4), it was found that the average bearing capacity of the rough interface group was 1262.2 kN, which corresponds to a stress of 126 MPa. This stress level is comparable to the compressive strength of the post-cast specimen (135.01 MPa in Table 3). Consequently, the stiffness in three directions for the rough interface group, represented as K_{nn}, was directly considered as a material parameter, and its value was determined to be 45820.
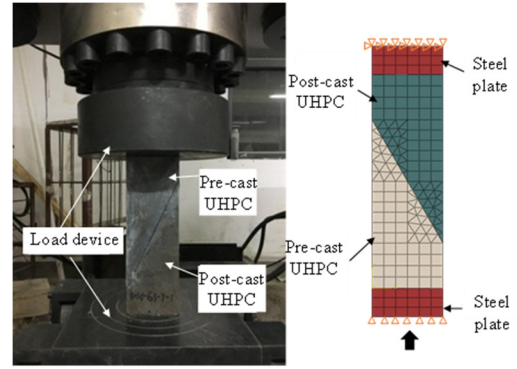

Fig. 20 Finite element model of oblique shear test

By using the relationship $G = E / 2(1 + v)$ between the elastic modulus and shear modulus, K_{ss} and K_{tt} were calculated and found to be 19092. The total plastic separation distance was obtained through fitting based on the experimental results, while the damping coefficient was set to 0.001. Therefore, in the computational model, only the total plastic separation distance needed adjustment. The finite element model, illustrated in Fig. 20, was utilized to present the final model parameters and fitting results, as shown in Table 6.

5. Numerical simulation of UHPC joint interface based on cohesion model

The simulation test in this paper can refer to Deng *et al.* (2021). The test is based on an actual UHPC bridge, and the materials used in the test are consistent with those described above.

5.1 Model establishment

The numerical simulation model is created in ABAQUS, incorporating various elements and contact parameters. The upper UHPC panel is represented by solid element C3D8R, while the lower I-beam is simulated using shell element S4R. The reinforcement in the UHPC panel is modeled using two-node three-dimensional truss element T3D2 and embedded within the UHPC panel using the "embedded region" feature. To simulate the stud connection between the UHPC panel and steel plate, spring elements are utilized, and a vertical coupling displacement is applied to prevent contact intrusion. The stiffness of the studs is determined based on the calculation formula specified in code GB50917-2013 (MOHURD 2013).

Two sets of contact parameters are implemented for the joint between the successively poured UHPC and precast

Table 6 Contact parameters of compression-shear dominated components

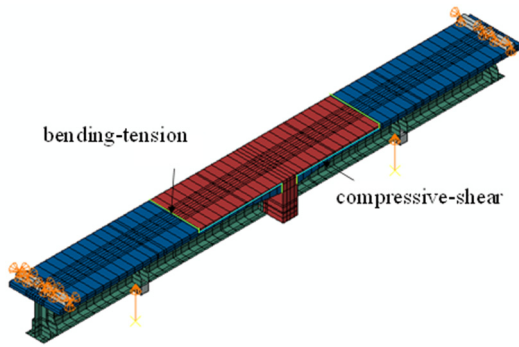| Interface form	$K_{nn}/K_{ss}/K_{tt}$	$t_n^0/t_s^0/t_t^0$ (MPa)	δp q(mm)	μ	Viscosity coefficient	Calculation results (kN)	Test result (kN)
Smooth	45820/19092/19092	17.49/30.31/30.31	0.03	1.62	0.001	696.54	700.22
Rough	45820/19092/19092	31.53/54.64/54.64	0.075	1.52	0.001	1241.39	1262.20

Fig. 21 Finite element model of joint test

slab. The parameters obtained from the interface bending test, as described earlier, are applied at the joint interface under bending and tension. Similarly, the parameters obtained from the interface oblique shear test are referenced for the part of the joint experiencing friction and shear. The schematic diagram of the finite element model is illustrated in Fig. 21, with the model set up in the forward direction

and the upward load applied. Steel base plates are placed on both sides and at the loading point to define the boundary conditions. Similar to the actual test, one side of the boundary condition is fixed, while the other side allows sliding. The material performance parameters remain consistent with the ones mentioned previously.

### 5.2 Applicability verification

Fig. 22 presents the test results of joint specimens and their comparison with the finite element model. In Fig. 22(a), it is evident that the front section of the load-displacement curve is well fitted. The stiffness of the test curve slightly decreases in the rear section due to multiple cracks in the UHPC panel. However, this phenomenon is not fully captured in the finite element model, resulting in a slightly higher calculated stiffness compared to the actual test results. The deflection at the peak point in the later stage of the calculation is slightly larger than the test value. Analysis of the test process indicates that this discrepancy is due to inaccurate setting of the reinforcement constitutive conditions. Nevertheless, the calculated ultimate load value
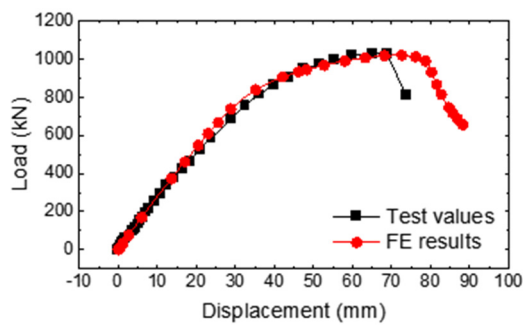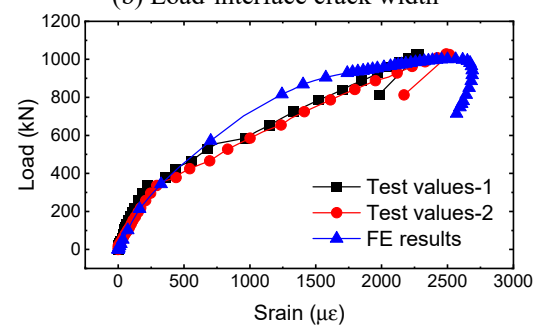
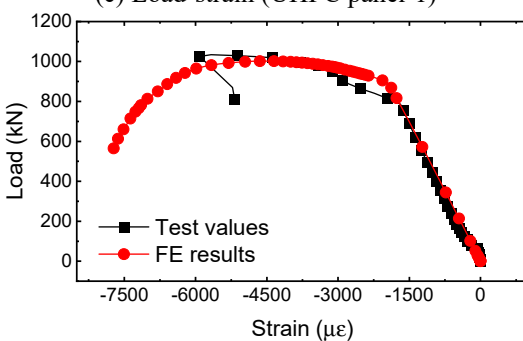

(a) Load-midspan displacement
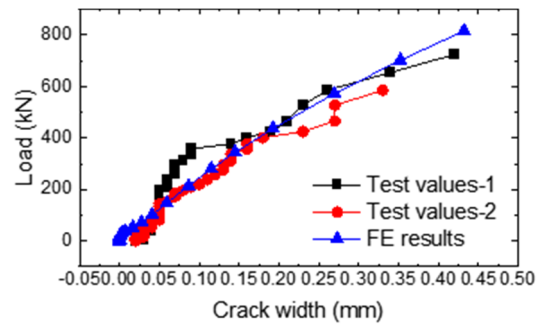
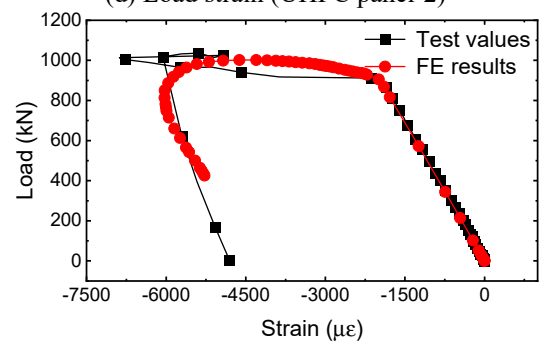(b) Load-interface crack width
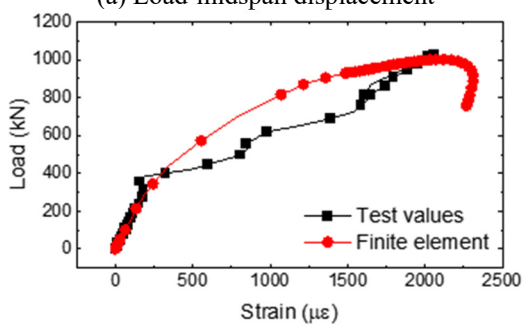
(c) Load-strain (UHPC panel-1)

(d) Load strain (UHPC panel-2)

(e) Load-strain (steel plate-1)

(f) Load strain (steel plate-2)

Fig. 22 Comparison between joint test results and finite element calculation values

(1020.2 kN) is slightly smaller than the test value (1033.9 kN), indicating a conservative approach and an acceptable calculation result.

Fig. 22(b) illustrates the fitting of crack width at the interface. The cohesive behavior is employed to simulate the interface behavior in the finite element model. The "COPEN" option is utilized to read the opening distance of the interface and fit the crack width. The results indicate that the front section of the calculated curve is slightly lower than the test value, demonstrating a conservative approach. However, when the crack width reaches 0.05 mm, the calculated load is 124.31 kN, which falls within the range of the test results (81.2-196.6 kN, with an average value of 138.9 kN). The calculated value aligns well with the test results, and the discrepancy with the average value is acceptable.

In Fig. 22(c), the calculated UHPC surface strain results show good agreement with the measured values in the front section. However, inaccuracies arise in the fitting due to the cracking of the UHPC panel, resulting in larger errors in the rear part. This suggests that the reliability of UHPC strain results obtained through strain gauges is questionable. Nevertheless, when cracking is not present in the early stage, the test results exhibit considerable reliability. Comparing the extensometer test results in Fig. 22(d), the finite element calculation better aligns with the entire loading process. Similar to the load midspan displacement curve fitting, the actual stiffness in the test is lower than the calculated results in the finite element model due to surface cracking of the UHPC panel in the rear section of the curve.

Figs. 22(e) and 22(f) show the comparison between the measured surface strain points in the steel structure and the calculated values from the finite element model. It is evident that the constitutive model of the steel structure exhibits good agreement with the test values, indicating a reliable representation of the actual steel constitutive behavior.

6. Conclusions

In this paper, the interface bending and oblique shear tests of two successively poured UHPC specimens with different roughness (smooth/rough) are carried out. By utilizing the cohesive model in ABAQUS, we obtained numerical simulation parameters and methods for the UHPC joint interface with bending-tension and compression-shear behaviors. Additionally, we discussed the determination method and influence range of each parameter. Based on our research, the main conclusions are as follows:

(1) The results of the interface flexural test revealed that the failure loads of the three smooth specimens were 8.34 kN, 9.52 kN, and 9.78 kN, respectively. On the other hand, the rough interface specimen displayed some variation in failure load and exhibited slight ductility, with ultimate loads of 34.52 kN, 15.62 kN, and 17.97 kN, respectively.

(2) The interface oblique shear test results indicated that the failure of smooth interface specimens occurred at the interface, with no visible damage in

the central core area. However, for the rough interface specimens, in addition to evident shear failure at the interface, partial crushing of the matrix was also observed. The average failure loads of smooth and rough tests were 700.215 kN and 1262.203 kN, respectively.

(3) The cohesive model in ABAQUS was used to fit the interfacial flexural and oblique shear tests. We successfully obtained numerical simulation parameters for the interfacial flexural-tensile and compressive-shear behaviors of UHPC joints based on the cohesive model. These parameters were validated against the successively poured joint test, and the results demonstrated good agreement.

References

Abokifa, M. and Moustafa, M.A. (2021), "Experimental behavior of precast bridge deck systems with non-proprietary UHPC transverse field joints", *Materials*, **14**(22), 6964. https://doi.org/10.3390/ma14226964

AFGC-SETRA (2013), Ultra high performance fibrereinforced concretes, Recommendations, Paris: AFGC&SETRA Working Group.

Bayat, M., Kia, M., Soltangharaei, V., Ahmadi, H.R. and Ziehl, P. (2020), "Bayesian demand model based seismic vulnerability assessment of a concrete girder bridge", *Adv. Concrete Constr., Int. J.*, **9**(4), 337-343. https://doi.org/10.12989/acc.2020.9.4.337

Birkeland, P.W. and Birkeland, H.W. (1966), "Connections in precast concrete construction", In: *Journal Proceedings*, Vol. 63, No. 3, pp. 345-368.

Cao, J.H. (2016), "Research on basic performance of steel-thin UHPC lightweight composite deck", Ph.D. Dissertation; Hunan University, Changsha, China.

Carbonell, M.A., Harris, D.K., Ahlborn, T.M. and Froster, D.C. (2014), "Bond performance between ultrahigh-performance concrete and normal-strength concrete", *J. Mater. Civil Eng.*, **26**(8), 04014031. https://doi.org/10.1061/(ASCE)MT.1943-5533.0000890

Chen, D. and El-Hacha, R. (2015), "Investigation of hybrid FRP-UHPC beams under flexure with finite element method", In: *International Concrete - Special Publication*, **301**, 1-16. https://doi.org/10.14359/51687993

Chen, L. and Graybeal, B.A. (2011), "Finite Element Modeling of Ultra-High-Performance Concrete Bridge Girders", Transportation Research Board Meeting.

Chen, L. and Graybeal, B.A. (2012a), "Modeling structural performance of ultrahigh performance concrete I-girders", *J. Bridge Eng.*, **17**, 754-764. https://doi.org/10.1061/(ASCE)BE.1943-5592.0000305

Chen, L. and Graybeal, B.A. (2012b), "Modeling structural performance of second-generation ultrahigh-performance concrete pi-girders", *J. Bridge Eng.*, **17**(4), 634-643. https://doi.org/10.1061/(ASCE)BE.1943-5592.0000301

Chitty, F.D., Freeman, C.J. and Garber, D.B. (2020), "Joint design

optimization for accelerated construction of slab beam bridges", *J. Bridge Eng.*, **25**(7), 04020029. https://doi.org/10.1061/(ASCE)BE.1943-5592.0001561

Dadmand, B., Pourbaba, M., Sadaghian, H. and Mirmiran, A. (2020), "Effectiveness of steel fibers in ultra-high-performance fiber-reinforced concrete construction", *Adv. Concrete Constr., Int. J.*, **10**(3), 195-209. https://doi.org/10.12989/acc.2020.10.3.195

Deng, S., Shao, X., Yan, B., Wang, Y. and Li, H. (2020), "On flexural performance of girder-to-girder wet joint for lightweight steel-UHPC composite bridge", *Appl. Sci.*, **10**, 1335. https://doi.org/10.3390/app10041335

Deng, S., Shao, X., Yan, B., Zhao, X. and Wang, Y. (2021), "Transverse joint design of small–medium-span fully precast steel–UHPC lightweight composite bridge", *J. Bridge Eng.*, **26**(8), 04021046. https://doi.org/10.1061/(ASCE)BE.1943-5592.0001745

Deng, E.F., Zhang, Z., Zhang, C.X., Tang, Y., Wang, W., Du, Z.J. and Gao, J.P. (2023), "Experimental study on flexural behavior of UHPC wet joint in prefabricated multi-girder bridge", *Eng. Struct.*, **275**, 115314. https://doi.org/10.1016/j.engstruct.2022.115314

Dias-da-Costa, D., Alfaiate, J. and Júlio, E.N.B.S. (2012), "FE modeling of the interfacial behaviour of composite concrete members", *Constr. Build. Mater.*, **26**(1), 233-243. https://doi.org/10.1016/j.conbuildmat.2011.06.015

Du, L., Qi, J., Cheng, Z. and Wang, J. (2022), "Finite element modeling of UHPC slabs with dovetail joints and steel wire mesh using an innovative interfacial treating method", In: *Structures*, **37**, 745-755 https://doi.org/10.1016/j.istruc.2022.01.057

Elices, M., Guinea, G.V. and Planas, J. (1992), "Measurement of the fracture energy using three-point bend tests: Part 3—influence of cutting the P-δ tail", *Mater. Struct.*, **25**, 327-334. https://doi.org/10.1007/BF02472591

Farzad, M., Shafieifar, M. and Azizinamini, A. (2019), "Experimental and numerical study on bond strength between conventional concrete and Ultra High-Performance Concrete (UHPC)", *Eng. Struct.*, **186**, 297-305. https://doi.org/10.1016/j.engstruct.2019.02.030

Ganesh, P. and Murthy, A.R. (2019), "Repair, retrofitting and rehabilitation techniques for strengthening of reinforced concrete beams-A review", *Adv. Concrete Constr., Int. J.*, **8**(2), 101-117. https://doi.org/10.12989/acc.2019.8.2.101

Grace, N.F., Enomoto, T., Abdel-Mohti, A., Tokal, Y. and Puravankara, S. (2008), "Flexural behavior of precast concrete box beams post-tensioned with unbonded, carbon-fiber-composite cables", *PCI J.*, **53**(4).

Grace, N., Ushijima, K., Baah, P. and Bebawy, M. (2013), "Flexural behavior of a carbon fiber–reinforced polymer prestressed decked bulb T-beam bridge system", *J. Compos. Constr.*, **17**(4), 497-506. https://doi.org/10.1061/(ASCE)CC.1943-5614.0000345

Graybeal, B. (2014), *Design and Construction of Field-cast UHPC Connections*, (No. FHWA-HRT-14-084; HRDI-40/10-14 (750) E), Federal Highway Administration, United States.

Hájek, R., Horníková, K. and Foglar, M. (2020) "Numerical assessment of the response of a heterogeneous concrete-based composite bridge deck to a near field explosion", *Eng. Struct.*, **225**, 111206. https://doi.org/10.1016/j.engstruct.2020.111206

Han, J.H. (2002), "Research on Bonding Fracture Behavior of Old and New Concrete and Engineering Application", Ph.D. Dissertation; Dalian University of Technology, Dalian, China.

Han, J.H., Zhao, G.F. and Zhang, L.S. (2004), "Study of the fracture process zone of adhesive interface of new and old concrete", *Eng. Mech.*, **21**, 31-35.

Harris, D., Muñoz, M.C., Gheitasi, A., Ahlborn, T. and Rush, S. (2015), "The challenges related to interface bond

characterization of ultra-high-performance concrete with implications for bridge rehabilitation practices", *Adv. Civil Eng. Mater.*, **4**(2), 75-101. https://doi.org/10.1520/ACEM20140034

He, Z.-Q., Ma, Z.J., Chapman, C.E. and Liu, Z. (2013), "Longitudinal joints with accelerated construction features in decked bulb-tee girder bridges: Strut-and-tie model and design guidelines", *J. Bridge Eng.*, **18**, 372-379. https://doi.org/10.1061/(ASCE)BE.1943-5592.0000378

He, S., Mosallam, A.S., Fang, Z. and Liu, L. (2019), "Structural evaluation of steel–concrete joint with UHPC grout in single cable–plane hybrid cable-stayed bridges", *J. Bridge Eng.*, **24**, 04019022. https://doi.org/10.1061/(ASCE)BE.1943-5592.0001379

Hussein, H.H., Sargand, S.M., Al Rikabi, F.T. and Steinberg, E.P. (2017a), "Laboratory evaluation of ultrahigh-performance concrete shear key for prestressed adjacent precast concrete box girder bridges", *J. Bridge Eng.*, **22**, 04016113. https://doi.org/10.1061/(ASCE)BE.1943-5592.0000987

Hussein, H.H., Walsh, K.K., Sargand, SM., Al Rikabi, F.T. and Steinberg, E.P. (2017b), "Modeling the shear connection in adjacent box-beam bridges with ultrahigh-performance concrete joints. I: Model calibration and validation", *J. Bridge Eng.*, **22**, 04017043. https://doi.org/10.1061/(ASCE)BE.1943-5592.0001070

Hussein, H.H., Sargand, S.M., Zhu, Y., Khoury, I. and Al Rikabi, F.T. (2022), "Experimental and numerical investigation on optimized ultra-high performance concrete shear key with shear reinforcement bars", *Structures*, **40**, 403-419. https://doi.org/10.1016/j.istruc.2022.04.037

Jang, H.-O., Lee, H.-S., Cho, K. and Kim, J. (2018), "Numerical and experimental analysis of the shear behavior of ultrahigh-performance concrete construction joints", *Adv. Mater. Sci. Eng.*, **2018**, 1-17. https://doi.org/10.1155/2018/6429767

Jia, J., Ren, Z., Bai, Y., Li, J., Li, B., Sun, Y., Zhang, Z. and Zhang, J. (2023), "Tensile behavior of UHPC wet joints for precast bridge deck panels", *Eng. Struct.*, **282**, 115826. https://doi.org/10.1016/j.engstruct.2023.115826

Jiang, H., Hu, Z., Feng, J., Wang, T. and Xu, Z. (2022), "Flexural behavior of UHPC-filled longitudinal connections with non-contacting lap-spliced reinforcements for narrow joint width", *Structures*, **39**, 620-636. https://doi.org/10.1016/j.istruc.2022.03.017

Júlio, E.N., Branco, F.A., Silva, V.D. and Lourenço, J.F. (2006), "Influence of added concrete compressive strength on adhesion to an existing concrete substrate". *Build. Environ.*, **41**, 1934-1939. https://doi.org/10.1016/j.buildenv.2005.06.023

Katman, H.Y.B., Khai, W.J., Bheel, N., Kırgız, M.S., Kumar, A. and Benjeddou, O. (2022), "Fabrication and characterization of cement-based hybrid concrete containing coir fiber for advancing concrete construction", *Buildings*, **12**(9), 1450. https://doi.org/10.3390/buildings12091450

Larsson, J., Eriksson, P.E., Olofsson, T. and Simonsson, P. (2014), "Industrialized construction in the Swedish infrastructure sector: Core elements and barriers", *Constr. Manage. Econom.*, **32**(1-2), 83-96. https://doi.org/10.1080/01446193.2013.833666

Liao, Z. (2018), "Experimental research on bond strength of UHPC-NC interface", Master Dissertation; Hunan University, Changsha, China.

Lu, K., Xu, Q., Li, W., Hu, Y., Wang, J. and Yao, Y. (2021), "Fatigue performance of UHPC bridge deck system with field-cast dovetail joint", *Eng. Struct.*, **237**, 112108. https://doi.org/10.1016/j.engstruct.2021.112108

Mosaberpanah, M.A. and Eren, O. (2017), "Effect of quartz powder, quartz sand and water curing regimes on mechanical properties of UHPC using response surface modelling", *Adv. Concrete Constr., Int. J.* **5**(5), 481-492. https://doi.org/10.12989/acc.2017.5.5.481

MOHURD (2013), Code for design of steel and concrete composite bridges (GB50917-2013), China Planning Press, Beijing, China.

Pan, W.H., Fan, J.S., Nie, J.G., Hu, J.H. and Cui, J.F. (2016), "Experimental study on tensile behavior of wet joints in a prefabricated composite deck system composed of orthotropic steel deck and ultrathin reactive-powder concrete layer", *J. Bridge Eng.*, **21**, 04016064. https://doi.org/10.1061/(ASCE)BE.1943-5592.0000935

Pham, H.D., Khuc, T., Nguyen, T.V., Cu, H.V., Le, D.B. and Trinh, T.P. (2020), "Investigation of flexural behavior of a prestressed girder for bridges using nonproprietary UHPC", *Adv. Concrete Constr., Int. J.*, **10**(1), 71-79. https://doi.org/10.12989/acc.2020.10.1.071

Porter, S.D., Julander, J.L., Halling, M.W., Barr, P.J., Boyle, H. and Xing, S. (2011), "Flexural testing of precast bridge deck panel connections", *J. Bridge Eng.*, **16**, 422-430. https://doi.org/10.1061/(ASCE)BE.1943-5592.0000173

Qi, J., Bao, Y., Wang, J., Li, L. and Li, W. (2019), "Flexural behavior of an innovative dovetail UHPC joint in composite bridges under negative bending moment", *Eng. Struct.*, **200,** 109716. https://doi.org/10.1016/j.engstruct.2019.109716

Qi, J., Cheng, Z., Wang, J., Zhu, Y. and Li, W. (2020), "Full-scale testing on the flexural behavior of an innovative dovetail UHPC joint of composite bridges", *Struct. Eng. Mech., Int. J.*, **75,** 49-57. https://doi.org/10.12989/sem.2020.75.1.049

Qiu, M., Shao, X., Yan, B., Zhu, Y. and Chen, Y. (2022), "Flexural behavior of UHPC joints for precast UHPC deck slabs", *Eng. Struct.*, **251**, 113422. https://doi.org/10.1016/j.engstruct.2021.113422

Shah, Y.I., Hu, Z., Yin, B.S. and Li, X. (2021), "Flexural performance analysis of UHPC wet joint of prefabricated bridge deck", *Arab. J. Sci. Eng.*, **46,** 11253-11266. https://doi.org/10.1007/s13369-021-05735-z

Shao, X.D., Chen, B. and Zhou, X.H. (2017), "Experiment on bending behavior of wet joints in light-weighted composite deck system composed of steel and RPC layer", *China J. Highway Transport*, **30,** 210-217.

Shao, X.D., Hu, W.Y., Qiu, M.H., Wang, Y. and Zhao, X.D. (2021), "Experiment on flexural behavior of UHPC joint in negative moment area of composite bridges", *China J. Highway Transport*, **34,** 246-260.

Steinberg, E., Huffman, J., Ubbing, J. and Giraldo-Londoño, O. (2013), "Finite element modeling of adjacent prestressed concrete box-beams", *Proc., PCI National Bridge Conference, Precast/Prestressed Concrete Institute*, Chicago, IL, USA.

Systèmes, D. (2010), Abaqus 6.10: Analysis user's manual, Dassault Systèmes Simulia Corp., Providence, RI, USA.

Tan, Y., Lv, L.S., Zhang, D.W., Jin, W.L., Fang, M.S. and Li, S.H. (2022), "Fatigue performance of a simply-supported T-beam UHPC bridge deck variable section joint structure", *Eng. Struct.*, **269,** 114758. https://doi.org/10.1016/j.engstruct.2022.114758

Ulku, E., Attanayake, U. and Aktan, H.M. (2010), "Rationally designed staged posttensioning to abate reflective cracking on side-by-side box-beam bridge decks", *Transport. Res. Record*, **2172**, 87-95. https://doi.org/10.3141/2172-10

Wall, J. and Shrive, N. (1988), "Factors affecting bond between new and old concrete", *ACI Mater. J.*, **85,** 117-125.

Xiao, J.L., Guo, L.X., Nie, J.G., Li, Y.L., Fan, J.S. and Shu, B.A. (2022), "Flexural behavior of wet joints in steel-UHPC composite deck slabs under hogging moment", *Eng. Struct.*, **252**, 113636. https://doi.org/10.1016/j.engstruct.2021.113636

Yang, J. and Fang, Z. (2008), "Research on stress-strain relation of ultra high performance concrete", *Concrete*, **7**, 11-15.

Zhao, B. (2014), "Theoretical and experimental study on the constitutive relationship of HRB400 steel bar", Master Dissertation; Huazhong University of Science and Technology, China.

Zhao, C., Wang, K., Xu, R., Deng, K. and Cui, B. (2019a), "Development of fully prefabricated steel-UHPC composite deck system", *J. Struct. Eng.*, **145,** 04019051. https://doi.org/10.1061/(ASCE)ST.1943-541X.0002338

Zhao, M., He, X.D., Qiu, M.H., Yan, B.F. and Shao, X.D. (2019b), "Fully prefabricated steel-HUPC lightweight composite girder in medium and small span girder bridge", *Highway Eng.,* **44**(5)**,** 63-66. https://doi.org/10.19782/j.cnki.1674-0610.2019.05.013

Zhu, Y., Zhang, Y., Hussein, H.H. and Cai, S. (2020a), "Flexural study on UHPC–steel composite beams with joints under negative bending moment", *J. Bridge Eng.*, **25**(10), 04020084. https://doi.org/10.1061/(ASCE)BE.1943-5592.0001619

Zhu, Y., Zhang, Y., Hussein, H.H. and Chen, G. (2020b), "Flexural strengthening of reinforced concrete beams or slabs using ultra-high performance concrete (UHPC): A state of the art review", *Eng. Struct.*, **205**, 110035. https://doi.org/10.1016/j.engstruct.2019.110035

Zhu, Y., Zhang, Y., Hussein, H.H. and Chen, G. (2020c), "Numerical modeling for damaged reinforced concrete slab strengthened by ultra-high performance concrete (UHPC) layer", *Eng. Struct.*, **209**, 110031. https://doi.org/10.1016/j.engstruct.2019.110031

Zhu, Y., Zhang, Y., Hussein, H.H., Liu, J. and Chen, G. (2020d), "Experimental study and theoretical prediction on shrinkage-induced restrained stresses in UHPC-RC composites under normal curing and steam curing", *Cement Concrete Compos.*, **110**, 103602. https://doi.org/10.1016/j.cemconcomp.2020.103602

JK